



**Rapid Solidification for Green-Solvent-Processed Large-Area
Organic Solar Modules with >16% Efficiency**

Journal:	<i>Energy & Environmental Science</i>
Manuscript ID	EE-ART-02-2024-000680.R1
Article Type:	Paper
Date Submitted by the Author:	15-Mar-2024
Complete List of Authors:	<p>Zhang, Ben; Soochow University Chen, Weijie; Soochow University, College of Chemistry, Chemical Engineering and Materials Science Chen, Haiyang; Soochow University Zeng, Guang; Soochow University Zhang, Rui; Linköping University, IFM Li, Hongxiang; Sichuan University, College of Polymer Science and Engineering, State Key Laboratory of Polymer Materials Engineering Wang, Yunfei; University of Southern Mississippi, School of polymer science of engineering Gu, Xiaodan; University of Southern Mississippi, School of Polymer Science and Engineering Sun, Weiwei; Soochow University Gu, Hao; Soochow University Gao, Feng; Linköping University, Department of Physics, Chemistry and Biology (IFM) Li, Yaowen; Soochow University, College of Chemistry, Chemical Engineering and Materials Science Li, Yongfang; Chinese Academy of Sciences, Institute of Chemistry</p>

Broader context

Organic solar cells (OSCs) have the advantages in solution printability, light weight, and intrinsic flexibility, which promotes its widely deployable in photovoltaic building integration and self-powered flexible electronics. However, for the upscaling fabrication of green solvent-processed OSCs toward commercialization, the uncontrollable temperature-dependent fluid mechanics and solvent evaporation kinetics lead to the deteriorated uniformity of active layer, resulting in a huge scaling lag in module efficiency. In this study, we proposed a rapid solidification strategy to accelerate the evaporation of green solvent toluene at room temperature. This strategy solves the issues of molecular aggregation and Marangoni effect simultaneously in the green solvent blade-coating process, allowing the formation of a nano-scale phase separation active layer with uniform morphology. The resultant large-area OSC module achieve record power conversion efficiencies of 16.03% (15.64-cm²; certified: 15.69%) and 14.45% (72.00-cm²), showing a weak scale dependence.

Rapid Solidification for Green-Solvent-Processed Large-Area Organic Solar Modules with >16% Efficiency

Ben Zhang,^a Weijie Chen,^a Haiyang Chen,^a Guang Zeng,^a Rui Zhang,^d Hongxiang Li,^e Yunfei Wang,^f Xiaodan Gu,^f Weiwei Sun,^a Hao Gu,^a Feng Gao,^d Yaowen Li,^{*a,b,c} and Yongfang Li^{a,b,g}

^a *Laboratory of Advanced Optoelectronic Materials, Suzhou Key Laboratory of Novel Semiconductor-optoelectronics Materials and Devices, College of Chemistry, Chemical Engineering and Materials Science, Soochow University, Suzhou 215123, China*

Email: ywli@suda.edu.cn

^b *Jiangsu Key Laboratory of Advanced Negative Carbon Technologies, Soochow University, Suzhou 215123, China*

^c *State and Local Joint Engineering Laboratory for Novel Functional Polymeric Materials, Jiangsu Key Laboratory of Advanced Functional Polymer Design and Application, College of Chemistry, Chemical Engineering and Materials Science, Soochow University, Suzhou 215123, China*

^d *Department of Physics, Chemistry and Biology (IFM), Linköping University, Linköping SE-58183, Sweden*

^e *College of Polymer Science and Engineering, State Key Laboratory of Polymer Materials Engineering, Sichuan University, Chengdu 610065, China*

^f *School of Polymer Science and Engineering, Center for Optoelectronic Materials and Devices, The University of Southern Mississippi, Hattiesburg, Mississippi 39406, United States*

^g *Beijing National Laboratory for Molecular Sciences; CAS Key Laboratory of Organic Solids, Institute of Chemistry, Chinese Academy of Sciences, Beijing 100190, China*

Keywords:

Organic solar cells, Green solvents, Molecular aggregation, Marangoni effect, Rapid solidification

Abstract

Enabling green-solvent-processed large-area organic solar cells (OSCs) is of great significance to their industrialization. However, precisely controlling the temperature-dependent fluid mechanics and evaporation behavior of green solvents with high-boiling points is challenging. Controlling these parameters is essential to prevent non-uniform distribution of active layer components and severe molecule aggregation, which collectively degrade the power conversion efficiency (PCE) of large-scale devices. In this study, we revealed that the temperature gradient distribution across a wet film is the root of notorious Marangoni effect, which leads to the formation of a severely non-uniform active layer on large scale. Thus, a rapid solidification strategy was proposed to accelerate the evaporation of toluene, a green solvent, at room temperature. This strategy simultaneously inhibits the Marangoni effect and suppresses molecular aggregation in the wet film, allowing the formation of a nano-scale phase separation active layer with uniform morphology. The resultant toluene-processed 15.64-cm² large-area OSC module achieves an outstanding PCE of 16.03% (certified: 15.69%), which represents the highest reported PCE of green-solvent-processed OSC modules. Notably, this strategy also exhibits a weak scale dependence on the PCE, and we successfully achieved a state-of-the-art PCE of 14.45% for a 72.00-cm² OSC module.

1. Introduction

Benefiting from the rapid development of A-DA'D-A-type small molecule acceptors, the power conversion efficiency (PCE) of small-area organic solar cells (OSCs) has skyrocketed to 19.6%, reaching the threshold of commercialization.¹ However, the PCE drops significantly upon upscaling of device areas owing to uniformity deterioration of the active layer.²⁻⁴ In addition, these active layers are usually processed from a toxic solvent chloroform (CF), which incompatible with industrial production.⁵⁻⁷ Therefore, developing highly efficient large-area OSC modules using green solvents is necessary.

An ideal large-area active layer of OSC module should exhibit a uniform and nano-scale phase-separated morphology.^{8, 9} However, the boiling points of green solvents, such as commonly used toluene (PhMe) and *o*-xylene (*o*-XY), are usually significantly higher than that of the toxic solvent CF. The related slow evaporation rate of the solvent can interfere with the molecular crystallization process and prolong film solidification time, finally resulting in the formation of an oversized domain or excessive phase separation in the active layer.^{10, 11} The resultant OSCs show large non-radiative recombination losses and an inferior photovoltaic performance.¹²⁻¹⁴ Vacuum-assisted annealing significantly accelerates solvent evaporation, leading to the formation of a smooth surface morphology with close molecular stacking.¹⁵ However, application of this method in large-area production is hindered by the challenges associated with the realization of a high vacuum degree. Instead, a hot substrate, which is a simple and efficient strategy, can accelerate the evaporation of solvents like *o*-XY in blade-coated PM6:Y6 active layer, which shows nano-scale phase separation with suppressed Y6 aggregation.¹⁶ Although high-temperature (HT) processing can efficiently mitigate molecular aggregation, it will bring a new issue in regulating the fluid mechanics of active layer solution.

Fluid mechanics commonly governing large-scale printing processes are determined by solution viscosity, shear rate, and especially substrate temperature.¹⁷⁻¹⁹ Generally, the solvent molecules at the gas-liquid interface, called the meniscus, are subjected to

interaction forces of other solvent molecules directed toward the liquid interior, thus generating surface tension (Supplementary discussion 1). And an elevated temperature can create a gradient temperature distribution along the meniscus from the substrate to the top, i.e., gas-liquid-solid three-phase contact line (TCL) is much higher than that on the solution top surface. Then, the temperature-dependent interaction force of the solvent molecules leads to the formation of a temperature/surface tension gradient along the meniscus. In this case, the Marangoni flow occurs at the meniscus from the low (near substrate)-to-high (top surface) surface tension region.^{20, 21} During the film forming process, the organic solutes continuously move away from the TCL along the Marangoni flow, leading to a heterogeneous distribution of molecules and non-uniform film. Therefore, tremendous efforts have been devoted to solvent and substrate engineering for suppressing the Marangoni effect during large-area printing.^{20, 22, 23} For example, Chan et al.²⁴ proposed the use of mixed solvents (*m*-xylene and *o*-dichlorobenzene) to change the direction of the Marangoni flow. *o*-dichlorobenzene could accumulate near the TCL owing to its lower volatility than that of *m*-xylene. Benefiting from the higher surface tension of *o*-dichlorobenzene, the organic solutes at the mixed solvent region are pulled to the TCL, leading to the formation of a continuous and uniform film. Zhao et al.²⁵ demonstrated that moderate heating can reduce the temperature gradient, thus alleviating the Marangoni effect. However, the above-mentioned strategies cannot completely eliminate the adverse Marangoni effect. Therefore, developing a simple strategy to inhibit molecular aggregation while eliminating the Marangoni effect is imperative to enhance molecular crystallinity and ensure the formation of a uniform film morphology on large scales.

In this study, we revealed that the Marangoni effect induced heterogeneous components distribution and non-uniform film can be triggered at a heated substrate even as low as 40°C. For the films processed with high-boiling point green solvents, we proposed a rapid solidification (RS) strategy at room temperature (RT), which could precisely control the solvent evaporation rate by modulating the airflow velocity over

the wet film. This RS strategy accelerates solvent evaporation without heating and effectively suppresses molecular aggregation. In addition, the RT processing could avoid temperature/surface tension gradient, thus inhibiting the Marangoni effect. These advantageous features of the RS strategy contributed to the formation of a continuous film with nano-scale phase-separated morphology and preferred face-on orientation. The resultant small-area OSCs exhibited a champion PCE of 18.22% when using a green solvent PhMe, and maintained 88.5% of its initial PCE after maximum power point (MPP) tracking for 1000 h. Notably, a 15.64-cm² OSC module delivered an outstanding PCE of 16.03% (certified 15.69%), which is the highest efficiency of green-solvent-processed large-area OSC modules reported thus far. Furthermore, a 72.00-cm² large-area OSC module, fabricated using the RS strategy, also exhibited a remarkable PCE of 14.45%.

2. Results and Discussion

A representative high-efficiency PM6:D18:L8-BO ternary system was selected as the active layer in this study, in considering its good film-formation characteristics in PhMe green solvent (Figure 1a), and the blade-coating technique in ambient condition with a relative humidity ~40% was employed.^{26, 27} However, the solvent evaporation rate of PhMe, which has a high-boiling point of ~110°C, needs to be increased using a HT process for suppressing oversized domain or excessive phase separation.^{28, 29} Here, a finite element model was constructed to simulate the temperature distribution across the film (Figure 1b), and the substrate temperature was maintained at 40°C.^{30, 31} The region near the TCL shows a higher temperature and gradually decreases along the meniscus from the bottom to the top, resulting in an increased surface tension gradient. Moreover, the simulated results of the solution flow velocity distribution across the wet film, where the flow velocity in the top meniscus exceeds that near the TCL (Figure 1c), confirm the occurrence of the Marangoni flow. It would make organic solute move away from TCL (Figure S1, Supporting Information (SI)), thus causing heterogeneous component distribution.²²

To reveal the influence of temperature gradient on the Marangoni effect, the Marangoni number (Ma), which quantitatively reflects the strength of the Marangoni effect along the meniscus, was calculated using the following equation:^{25, 32}

$$Ma = -\frac{d\gamma}{dT} \frac{\Delta TL}{\mu\alpha}$$

where γ is the surface tension, ΔT is the temperature difference across the wet film, L is the thickness of the wet film, μ is the dynamic viscosity, and α is the thermal diffusivity. The surface tension of the PM6:D18:L8-BO film under different substrate temperatures is determined via contact angle measurement (Figure S2, SI),³³ and the calculated surface tension coefficient $d\gamma/dT$ is $-0.059 \text{ mN}\cdot\text{m}^{-1}\cdot\text{K}^{-1}$ (Figure S3 and Table S1, SI). The values of ΔT , L , μ , and α at different substrate temperatures were measured and listed in Table S2, SI. The calculated Ma values for the PM6:D18:L8-BO system

Inset: schematic illustration of the surface tension gradient along the meniscus. **c)** Simulation of the velocity distribution along the meniscus. **d)** Marangoni number of the wet films at different substrate temperatures; the critical value is 80. **e)** Evaporation rate versus airflow velocity and the corresponding optical microscope images of the active layer. Inset: schematic illustration of the effect of airflow over the wet film on the solution evaporation.

To eliminate the Marangoni effect, we proposed an RS strategy that regulates the airflow velocity over the wet films at RT. According to the Bernoulli equation, a high airflow velocity causes a large atmospheric pressure gradient from the solution surface (gas-liquid interface or meniscus) to the airflow layer, and this gradient continuously drives solvent evaporation (Figure 1e).³⁶ To quantify the effect of airflow velocity on the evaporation rate of the PhMe solvent, the Dalton evaporation empirical formula was used.^{37, 38}

$$\omega = 0.22 \times (E - e) \times \sqrt{1 + 0.32 \times v^2}$$

where ω is the evaporation rate, E is the saturated vapor pressure of the solvent, e is the vapor pressure above the solution, and v is the airflow velocity measured using an anemometer (Figure S5, SI). The calculated PhMe solvent evaporation rates for airflow velocities of 3.87, 5.32, and 8.26 m/s are 8.5, 11.2, and 16.8 mm/d, respectively (Figure 1e, Table S3 and Supplementary discussion 2, SI). It is also important to note that variations in airflow velocities do not influence the location of the TCL (Figure S6, SI). An optical microscope was used to visually distinguish the crystallization of the corresponding blend films, where the as-cast films were further annealed for sufficiently assembling (Figure 1e and Supplementary discussion 3, SI).³⁹ Evidently, the film processed at a low evaporation rate (8.5 mm/d) exhibits a small number of large-sized crystals, which are possibly formed because of severe molecular aggregation. In contrast, the film processed at a high evaporation rate (16.8 mm/d) exhibits numerous tiny-size crystals. This significant difference may be ascribed to the varied supersaturation time that determined by the evaporation rate, then influencing the subsequent nucleation density and growth rate. A low evaporation rate is known to

extend the supersaturation time, thus limiting the number of nucleation sites and retarding the crystal growth rate; a high evaporation rate can shorten the supersaturation time, causing direct precipitation of the organic solute without sufficient assembly.⁴⁰⁻⁴² Notably, a moderate evaporation rate of 11.2 mm/d can provide an optimal balance between the supersaturation time and nucleation density, and consequently, medium-sized needle-type crystals are formed under this condition.⁴³ This result reveals that the RS strategy with a moderate evaporation rate is expected to form favorable aggregation sizes.

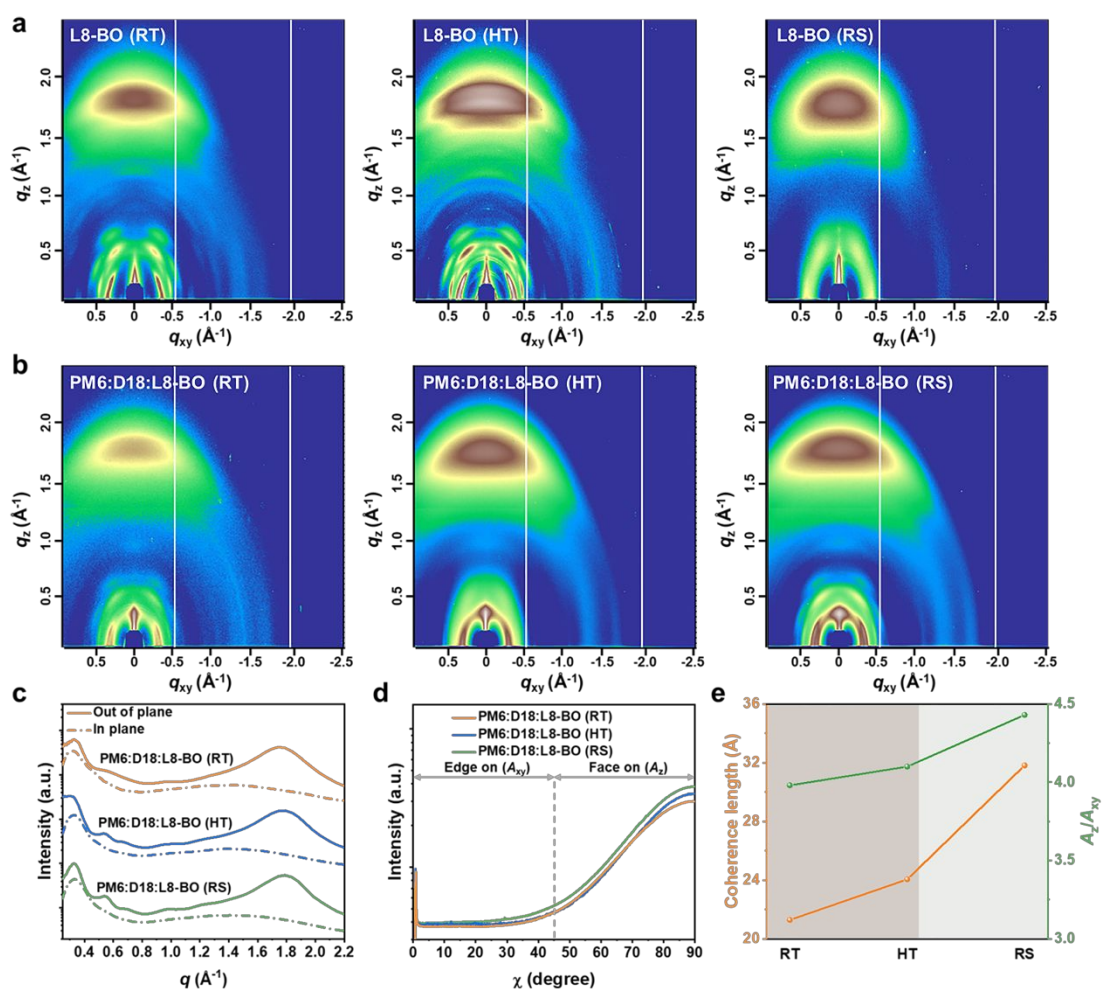


Figure 2. a) 2D GIWAXS patterns of the L8-BO and b) PM6:D18:L8-BO films fabricated using different processing methods. c) Integrated scattering profiles of the PM6:D18:L8-BO films, fabricated using different processing methods, along the IP and OOP directions. d) Corresponding pole figures extracted from the (010) diffraction patterns. e) Calculated A_z/A_{xy} and CCL values of the (010) diffraction patterns in the q_z direction.

In addition, to in-depth evaluation of the various film-formation processes, i.e., RT (25°C), HT (40°C), and RS (25°C), the crystallization behavior was first investigated, where the film processed using the RS strategy at a fixed solvent evaporation rate of 11.2 mm/d. Ultraviolet--visible (UV-vis) absorption spectra of single component, respective donor or acceptor, neat films were measured to understand which component is susceptible to fluid mechanics and solvent evaporation kinetics. The characteristic spectra of neat PM6 and D18 films are almost consistent irrespective of the processing methods (Figures S7a-b, SI) because the polymer crystallization is mainly determined by its pre-aggregation in solution.⁴⁴⁻⁴⁶ Besides, 2D grazing incidence wide angle X-ray scattering (2D GIWAXS) measurement was conducted to assess the polymer crystallization. As shown in Figure S8, SI, the PM6 and D18 films fabricated using different processing methods display minor changes in both in-plane (IP) and out-of-plane (OOP) directions, thus delivering similar *d*-spacing and crystal coherence lengths (CCLs) (Figure S9 and Tables S4-S5, SI). This once again indicates the crystallization behavior of polymer is not sensitive to the processing methods. By contrast, the 0-0 peaks of RT- and HT-processed neat L8-BO films exhibit approximately 11 nm and 8 nm red-shift respectively in comparison with that of RS-processed one (Figure S7c, SI). Further, the intensity of the 0-1 shoulder peak of the RS-processed film is significantly suppressed. These results confirm that the disordered aggregation caused by the slow solvent evaporation at RT (25°C) or HT (40°C) with adverse Marangoni effect are suppressed in the RS-processed films.⁴⁷ To further quantify the effect of the different processing methods on the crystallinity of L8-BO, the GIWAXS measurement was performed (Figure 2a). Both RT- and HT-processed L8-BO films exhibit multiple diffraction patterns in different directions, whereas the RS-processed film shows only one type of predominant π - π stacking diffraction pattern at 1.80 Å⁻¹ in the OOP (010) direction. In detail (Figure S10a and Tables S4-S5, SI), compared to the RT- and HT-processed films, RS-processed L8-BO film exhibits a relatively large CCL value of (010) peak in OOP direction and a smaller *d*-spacing distance. Those result further

confirm that the RS-processed film shows suppressed disordered aggregation and enhanced π - π stacking of L8-BO molecule. To investigate the corresponding changes in molecular orientation, pole figures were extracted from the graph of (010) peak intensity versus polar angle (χ). The χ values in the ranges of 0-45° (A_{xy}), and 45-90° (A_z) indicate the corresponding fractions of edge-on and face-on crystallites, respectively.⁴⁸ As shown in Figure S10b, SI, the RS-processed L8-BO film shows a large A_z/A_{xy} value of 4.98 (Figure S10b and Table S6, SI), which exceeds those of the RT- and HT-processed L8-BO films (3.94 and 4.20, respectively). All the discussions above confirm that the RS strategy could induce L8-BO to preferentially form a face-on orientation with enhanced long-range ordered molecular stacking (high crystallinity).

To assess whether the enhanced crystallinity of L8-BO remained when mixing with the donors, 2D GIWAXS measurements of the blend films (PM6:D18:L8-BO) processed by various methods were further conducted (Figure 2b). The RS-processed blend film exhibits enhanced intensities in both IP (100) and OOP (010) direction, and the corresponding CCL values (57.73 and 31.81 Å, respectively) are higher than those of RT- (34.71 and 43.85 Å, respectively) and HT- (21.28 and 24.05 Å, respectively) processed blend films (Figure 2c and Tables S7-S8, SI). In addition, the A_z/A_{xy} value of the RS-processed blend film (4.43; Figures 2d-e and Table S9, SI) is larger than those of the RT- and HT-processed blends (3.98 and 4.10, respectively). These suggest that the RS strategy can also assist in L8-BO crystallization with a more ordered arrangement and preferred face-on orientation even in the PM6:D18:L8-BO ternary active layer.

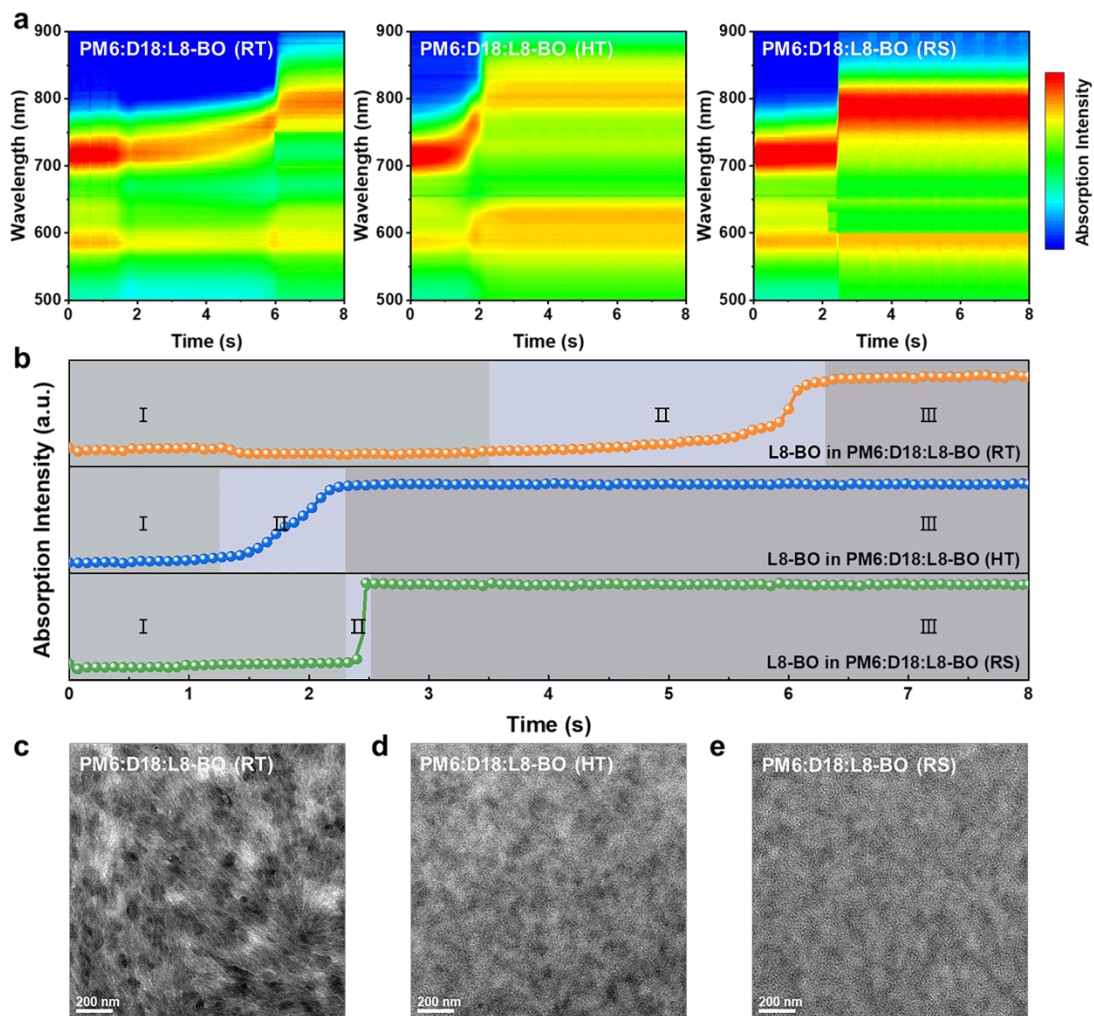


Figure 3. **a)** *In-situ* UV-vis absorption spectra of the PM6:D18:L8-BO films fabricated using different processing methods. **b)** Changes in the intensity of ~ 790 nm absorption peak of L8-BO in PM6:D18:L8-BO. **c-e)** TEM images of the PM6:D18:L8-BO films fabricated using different processing methods.

To evaluate the mechanism underlying the active layer growth using the RS strategy, the film-formation process was tracked using the *in-situ* UV-vis absorption characterization. The detected absorption peaks at 400-650 nm and 650-980 nm are characteristic features of PM6:D18 and L8-BO, respectively (Figures 3a and S11-S12, SI). The film forming process can be divided into three different stages: (I) solvent evaporation, (II) molecular crystallization, and (III) film solidification. A significant difference is observed in the crystallization stage of L8-BO; the crystallization times of the RT-, HT-, and RS-processed films are 2.80, 1.05, and 0.30 s, respectively (Figure S13, SI). The notably shortened crystallization time of RS-processed blend film

suggests a fast crystallization rate (Figures 3b and S14, SI), thus enhancing the L8-BO crystallinity in the blend film.^{28, 49} Subsequently, the impact of molecular crystallization on the microstructure morphology of blend films fabricated using various processing methods were investigated via atomic force microscopy (AFM) and transmission electron microscopy (TEM). The RT-based film exhibits a large root-mean-square roughness (RMS) of 6.52 nm (Figure S15a, SI) as well as large domain sizes (Figure 3c), which can be attributed to the molecular aggregation caused by the slow solvent evaporation at RT. Although the HT can mitigate this behavior as evidenced from the reduced RMS surface and weakened phase separation, a heterogeneous phase distribution still exists in the film (Figures 3d and S15b, SI), which may hinder charge transport and extraction. Contrarily, the RS-processed blend film exhibits a well-mixed interpenetrating network structure with optimized domain sizes (Figures 3e and S15c, SI). Such a morphology is beneficial for exciton dissociation and charge transport and is thus suitable for facilitating uniform and large-scale active layers.⁵⁰

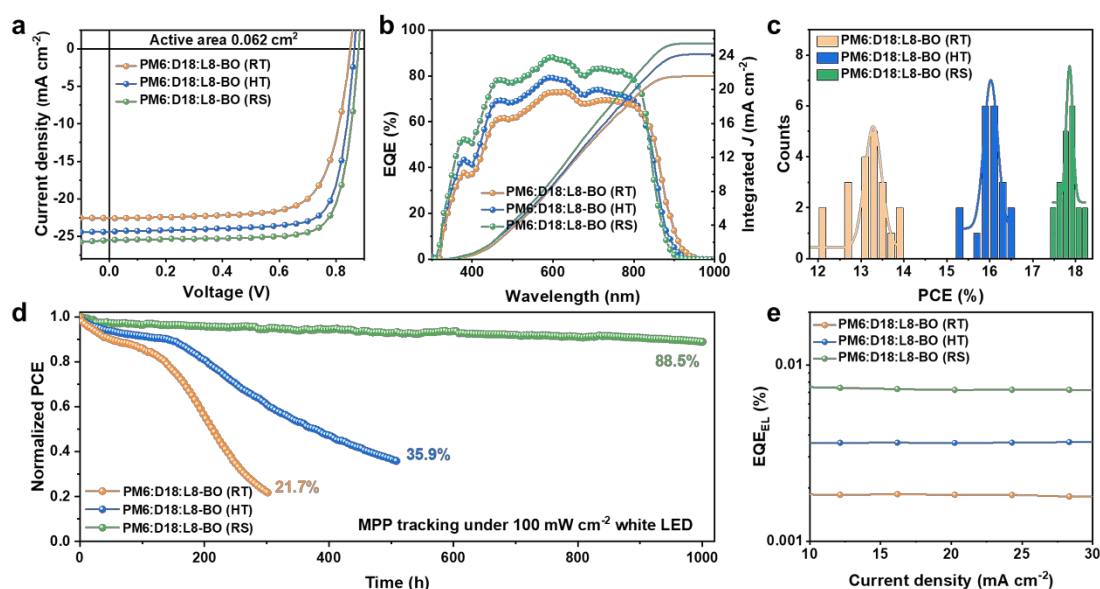


Figure 4. a) $J-V$ curves of the PM6:D18:L8-BO-based OSCs, subjected to various processing methods, under AM 1.5G illumination with an intensity of 100 mW cm^{-2} . b) Corresponding EQE spectra. c) Histograms of the PCE counts of 20 individual PM6:D18:L8-BO-based OSCs subjected to various processing methods. d) MPP stability test of the unencapsulated OSCs based on PM6:D18:L8-BO, subjected to various processing methods and stored in N_2 atmosphere, under the illumination of a

100 mW cm⁻² white LED. e) EQE_{EL} spectra of the PM6:D18:L8-BO-based OSCs subjected to various processing methods.

Based on the above-mentioned investigation, OSCs with a configuration of indium tin oxide (ITO)/Al-doped ZnO (AZO)/PM6:D18:L8-BO/MoO₃/Al were fabricated, and the active layers were processed using the RT, HT, and RS with PhMe as the solvent. The current density–voltage (J – V) curves and related photovoltaic parameters are presented in Figures 4a, S16–S17 and Tables 1, S10–S11, SI. The RS-based 0.062-cm² OSC exhibits a remarkable PCE of 18.22%, with an open-circuit voltage (V_{oc}) of 0.895 V, short-circuit current density (J_{sc}) of 25.62 mA cm⁻², and fill factor (FF) of 79.50%; this PCE surpasses those of the RT- and HT-based OSCs (13.82% and 16.50%). The external quantum efficiency (EQE) spectra show that the integrated J_{sc} values of the corresponding OSCs agree well with those obtained from the J – V curves within 5% deviation (Figure 4b). Notably, compared to the RT- and HT-based OSCs, the RS-based OSCs show a higher average PCE of 17.83% and a narrower distribution (Figure 4c). The operational stabilities under continuous MPP tracking reveal that the RS-based OSCs can maintain 88.5% of its initial PCE after 1000 h (Figure 4d). In contrast, the RT- and HT-based OSCs can maintain only 21.7% and 35.9%, respectively. These results collectively suggest that the RS strategy can help finetune the film morphology by suppressing the L8-BO aggregation and inhibiting Marangoni effect, which is benefit in forming nano-scale phase-separated morphology and enhancing the crystallization, thus improving the photovoltaic efficiency and operational stability.⁵¹ More importantly, the RS strategy shows good universality for other green solvent (*o*-XY and 1,2,4-trimethylbenzene)-processed active layers. The resultant devices show outstanding PCEs of ~17%, which is significantly higher than those of their RT and HT counterparts (Figure S18 and Tables S12–S13, SI).

Next, the mechanism underlying the observed high photovoltaic performance of the RS-based OSCs was evaluated. The voltage differences of the devices were analyzed by evaluating energy loss using the detailed balance theory.⁵² Based on the optical

bandgap and highly sensitive EQE values, the three devices exhibited similar ΔE_1 and ΔE_2 values (Figure S19, Table S14 and Supplementary discussion 4, SI). The RS-based device showed a significantly higher external electroluminescence quantum efficiency (EQE_{EL}) (Figure 4e and Table S14, SI), leading to a considerable reduction in ΔE_3 to 0.245 eV, compared to 0.281 and 0.262 eV for the RT- and HT-based devices, respectively. This result demonstrates that the RS strategy can more effectively suppress non-radiative recombination owing to the improved L8-BO crystallinity.⁵³⁻⁵⁶ Moreover, because of the high and more balanced hole/electron mobility in the RS-based OSCs, space-charge accumulation is reduced, and the FF of the device is enhanced. This result is consistent with the observed nano-scale phase-separated morphology and even component distribution (Figure S20 and Table S15, SI). In addition, the prolonged photovoltage and shortened photocurrent decay lifetimes for the RS-based OSCs indicate a long carrier lifetime and more efficient carrier extraction in the device, which correlate with suppressed aggregation and recombination (Figure S21, SI). In summary, the improved carrier dynamic behaviors strongly underpin the nano-scale phase-separated morphology and effective charge transport channels in the RS-based OSCs, and can well explain its superior photovoltaic parameters.

Table 1. Photovoltaic parameters of small-area OSCs.

Active layer	V_{oc} (V)	J_{sc} (mA cm^{-2})	$J_{\text{calc}}^{\text{a)}$ (mA cm^{-2})	FF (%)	PCE (%)
PM6:D18:L8-BO (RT)	0.845 (0.840 ± 0.003)	22.54 (22.12 ± 0.37)	21.55	72.50 (72.06 ± 0.45)	13.82 (13.15 ± 0.50)
PM6:D18:L8-BO (HT)	0.867 (0.861 ± 0.004)	24.43 (24.10 ± 0.26)	24.16	77.97 (77.28 ± 0.36)	16.50 (16.08 ± 0.32)
PM6:D18:L8-BO (RS)	0.895 (0.892 ± 0.003)	25.62 (25.40 ± 0.17)	25.43	79.50 (79.38 ± 0.14)	18.22 (17.83 ± 0.21)

^{a)} The J_{calc} values were calculated from the EQE spectra. Note: the optimum parameters are given as the mean ± standard deviation in parentheses, based on calculations from 20 individual devices.

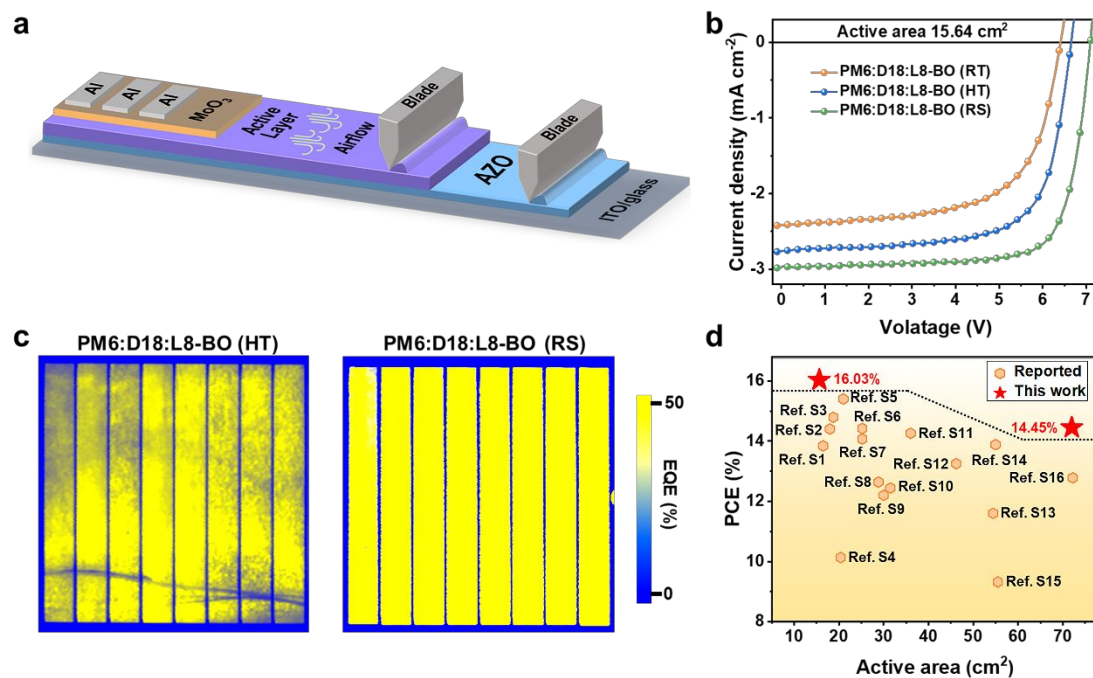


Figure 5. **a)** Schematic illustration of the RS blade-coating process for large-area OSC modules. **b)** J - V curves of the OSC modules under AM 1.5G illumination with an intensity of 100 mW cm^{-2} . **c)** LBIC mapping images of the HT- and RS-based OSC modules. The color scale bar represents the EQE intensity. **d)** Reported PCEs of green-solvent-based OSC modules with an active area over 10 cm^2 .

To assess the compatibility of the RS strategy with large-area printing, the PM6:D18:L8-BO-based 15.64-cm^2 OSC modules were fabricated with eight series-connected sub-cells (Figures S22-S23, SI). Figure 5a illustrates the RS process of the OSC modules under an ambient atmosphere (more details see Experimental Section in SI). The RS-processed 15.64-cm^2 OSC module exhibits an outstanding PCE of 16.03% with a V_{oc} of 7.09 V, J_{sc} of 2.97 mA cm^{-2} , and FF of 76.17%, and this PCE is significantly higher than those of the RT- and HT-based modules (9.96% and 12.94%, respectively; Figure 5b and Table 2). The light-beam-induced current (LBIC) mapping results and photographs of the OSC modules indicate that the photocurrent distribution and response of the RS-based module is more uniform than those of the RT- and HT-based modules (Figures 5c and S24-S25, SI), which is responsible for the improved photovoltaic parameters. This result was further confirmed by region-dependent optical absorption characterization of active layer film fabricated using different processing methods (Figure S26, SI), suggesting a high uniformity of RS-based film on a large-

scale. In addition, the influence of the different processing methods on the light stability of the OSC modules were examined by in nitrogen (N_2) atmosphere under the illumination of a light-emitting diode (LED). As shown in Figure S27, SI, RT- and HT-based OSC module only retained 60.4% and 81.6% of their initial PCEs after the light illumination for 206 h, respectively. In comparison, the RS-based OSC module could retain 92.8% of its initial PCE, indicating that a well-defined nano-scale phase-separated active layer morphology can minimize the device degradation. Notably, the 16.03% PCE is the highest value reported thus far for over 10 cm^2 green-solvent-processed large-area OSC modules (Figure 5d and Table S16, SI). This high efficiency was also certified to be 15.69% by the Shanghai Institute of Microsystem and Information Technology, Chinese Academy of Sciences (SIMIT) (Figure S28, SI, and Table 2). Even if the module area is expanded to 72.00 cm^2 , a remarkable PCE of 14.45% is still achieved (Figure S29, SI), further confirming the great prospects of the RS strategy for constructing ultra-large-area OSC modules.

Table 2. Photovoltaic parameters of the OSC modules.

Active layer	V_{oc} (V)	J_{sc} (mA cm^{-2})	FF (%)	PCE (%)
PM6:D18:L8-BO (RT)	6.46	2.43	63.54	9.96
PM6:D18:L8-BO (HT)	6.68	2.75	70.39	12.94
PM6:D18:L8-BO (RS)	7.09	2.97	76.17	16.03
PM6:D18:L8-BO (RS) ^a	7.14	2.92	75.31	15.69

^a) Certified result by SIMIT.

3. Conclusion

In summary, we successfully developed an RS strategy at RT to solve the issues of molecular aggregation and Marangoni effect simultaneously in the green solvent blade-coating process. An in-depth analysis of the associated mechanism revealed that a moderate evaporation rate is beneficial for optimizing the molecular crystallization duration to avoid severe molecular aggregation. In addition, the RT processing without any temperature/surface tension gradient eliminates the Marangoni effect, thus leading

to a highly homogenous component distribution. Both advantages facilitated the formation of a nano-scale interpenetrating network morphology with face-on orientation in the active layer. The resultant PhMe-processed 15.64 cm² OSC module exhibits a record PCE of 16.03%. In addition, the RS strategy shows great compatibility with larger-area OSC modules (72.00 cm²), which delivered a remarkable PCE of 14.45%. We believe that this RS strategy can significantly contribute to the development of green-solvent-processed large-area OSC modules for industrial applications.

Author Contributions

Y.W.L., W.J.C., and H.Y.C. conceived the idea and guided the work. B.Z. designed the experiments; B.Z., G.Z., W.W.S., and H.G. fabricated the organic active layer films and devices, and measured their performance; Y.F.W., R.Z., H.X.L., and X.D.G. conducted the GIWAXS measurements and processed the data; Y.W.L., B.Z., W.J.C., and H.Y.C. analyzed all measured results. W.J.C., H.Y.C., F.G., and Y.F.L. help to revise the manuscript. All authors commented on this paper.

Conflict of Interest

The authors declare no conflict of interest.

Acknowledgements

This work was supported by the National Natural Science Foundation of China (Grant Nos. 52325307, 52273188, 22075194, 22309129), the Natural Science Foundation of the Jiangsu Higher Education Institutions of China (Grant No. 20KJA430010), the Priority Academic Program Development of Jiangsu Higher Education Institutions (PAPD), Collaborative Innovation Center of Suzhou Nano Science and Technology, and the Key Laboratory of Polymeric Materials Design and Synthesis for Biomedical Function, Soochow University, Sichuan Science and Technology Program

(2023NSFSC0990). 2D GIWAXS data were acquired at beamlines 7.3.3 at the Advanced Light Source, which is supported by the Director, Office of Science, Office of Basic Energy Sciences, of the U.S. Department of Energy (DE-AC02-05CH11231). H.X.L. thanks the support of the Shanghai Synchrotron Radiation Facility (SSRF), beamline BL02U2 for 2D GIWAXS measurements.

Notes and references

- 1 L. Zhu, M. Zhang, J. Xu, C. Li, J. Yan, G. Zhou, W. Zhong, T. Hao, J. Song, X. Xue, Z. Zhou, R. Zeng, H. Zhu, C. C. Chen, R. C. I. MacKenzie, Y. Zou, J. Nelson, Y. Zhang, Y. Sun, F. Liu, *Nat. Mater.*, 2022, **21**, 656-663.
- 2 B. Zhang, F. Yang, S. Chen, H. Chen, G. Zeng, Y. Shen, Y. Li, Y. Li, *Adv. Funct. Mater.*, 2022, **32**, 2202011.
- 3 J. Zhang, L. Zhang, X. Wang, Z. Xie, L. Hu, H. Mao, G. Xu, L. Tan, Y. Chen, *Adv. Energy Mater.*, 2022, **12**, 2200165.
- 4 R. Sun, Q. Wu, J. Guo, T. Wang, Y. Wu, B. Qiu, Z. Luo, W. Yang, Z. Hu, J. Guo, M. Shi, C. Yang, F. Huang, Y. Li, J. Min, *Joule*, 2020, **4**, 407-419.
- 5 R. Sun, T. Wang, X. Yang, Y. Wu, Y. Wang, Q. Wu, M. Zhang, C. J. Brabec, Y. Li, J. Min, *Nat. Energy*, 2022, **7**, 1087-1099.
- 6 S. Yoon, S. Park, S. H. Park, S. Nah, S. Lee, J.-W. Lee, H. Ahn, H. Yu, E.-Y. Shin, B. J. Kim, B. K. Min, J. H. Noh, H. J. Son, *Joule*, 2022, **6**, 2406-2422.
- 7 X. Meng, L. Zhang, Y. Xie, X. Hu, Z. Xing, Z. Huang, C. Liu, L. Tan, W. Zhou, Y. Sun, W. Ma, Y. Chen, *Adv. Mater.*, 2019, **31**, 1903649.
- 8 Y. Su, Z. Ding, R. Zhang, W. Tang, W. Huang, Z. Wang, K. Zhao, X. Wang, S. Liu, Y. Li, *Sci. China Chem.*, 2023, **66**, 2380-2388.
- 9 Y. Xie, H. S. Ryu, L. Han, Y. Cai, X. Duan, D. Wei, H. Y. Woo, Y. Sun, *Sci. China Chem.*, 2021, **64**, 2161-2168.
- 10 H. Zhao, H. B. Naveed, B. Lin, X. Zhou, J. Yuan, K. Zhou, H. Wu, R. Guo, M. A. Scheel, A. Chumakov, S. V. Roth, Z. Tang, P. Muller-Buschbaum, W. Ma, *Adv. Mater.*, 2020, **32**, 2002302.
- 11 L. Zhu, M. Zhang, G. Zhou, T. Hao, J. Xu, J. Wang, C. Qiu, N. Prine, J. Ali, W. Feng, X. Gu, Z. Ma, Z. Tang, H. Zhu, L. Ying, Y. Zhang, F. Liu, *Adv. Energy Mater.*, 2020, **10**, 1904234.
- 12 W. Zhao, Y. Zhang, S. Zhang, S. Li, C. He, J. Hou, *J. Mater. Chem. C*, 2019, **7**, 3206-3211.
- 13 W. Zhao, S. Zhang, Y. Zhang, S. Li, X. Liu, C. He, Z. Zheng, J. Hou, *Adv. Mater.*, 2018, **30**, 1704837.
- 14 S. Dong, K. Zhang, T. Jia, W. Zhong, X. Wang, F. Huang, Y. Cao, *EcoMat*, 2019, **1**, e12006.

- 15 W. Guan, D. Yuan, J. Wu, X. Zhou, H. Zhao, F. Guo, L. Zhang, K. Zhou, W. Ma, W. Cai, J. Chen, L. Ding, L. Hou, *J. Semicond.*, 2021, **42**, 030502.
- 16 Y. Li, H. Liu, J. Wu, H. Tang, H. Wang, Q. Yang, Y. Fu, Z. Xie, *ACS Appl. Mater. Interfaces*, 2021, **13**, 10239-10248.
- 17 Y. Zheng, R. Sun, M. Zhang, Z. Chen, Z. Peng, Q. Wu, X. Yuan, Y. Yu, T. Wang, Y. Wu, X. Hao, G. Lu, H. Ade, J. Min, *Adv. Energy Mater.*, 2021, **11**, 2102135.
- 18 B. Lin, X. Zhou, H. Zhao, J. Yuan, K. Zhou, K. Chen, H. Wu, R. Guo, M. A. Scheel, A. Chumakov, S. V. Roth, Y. Mao, L. Wang, Z. Tang, P. Müller-Buschbaum, W. Ma, *Energy Environ. Sci.*, 2020, **13**, 2467-2479.
- 19 X. Chen, R. Huang, Y. Han, W. Zha, J. Fang, J. Lin, Q. Luo, Z. Chen, C. Q. Ma, *Adv. Energy Mater.*, 2022, **12**, 2200044.
- 20 C. Tian, J. Zhang, Y. Shen, H. Zhang, Z. Zhang, D. Qiu, L. Zhang, Z. Wei, *Sol. RRL*, 2023, **7**, 2300349.
- 21 X. Gu, L. Shaw, K. Gu, M. F. Toney, Z. Bao, *Nat. Commun.*, 2018, **9**, 534.
- 22 J. A. Lim, W. H. Lee, H. S. Lee, J. H. Lee, Y. D. Park, K. Cho, *Adv. Funct. Mater.*, 2008, **18**, 229-234.
- 23 K. Chang, Y. Li, G. Du, M. Zhong, P. Yang, Y. Zhu, F. He, B. Mi, X. Zhao, W. Deng, *ACS Appl. Mater. Interfaces*, 2020, **12**, 27405-27415.
- 24 Z. Zhang, B. Peng, X. Ji, K. Pei, P. K. L. Chan, *Adv. Funct. Mater.*, 2017, **27**, 1703443.
- 25 Y. Fan, J. Fang, X. Chang, M.-C. Tang, D. Barrit, Z. Xu, Z. Jiang, J. Wen, H. Zhao, T. Niu, D.-M. Smilgies, S. Jin, Z. Liu, E. Q. Li, A. Amassian, S. Liu, K. Zhao, *Joule*, 2019, **3**, 2485-2502.
- 26 J. Xue, H. Zhao, B. Lin, Y. Wang, Q. Zhu, G. Lu, B. Wu, Z. Bi, X. Zhou, C. Zhao, G. Lu, K. Zhou, W. Ma, *Adv. Mater.*, 2022, **34**, 2202659.
- 27 H. Lu, G. Ran, Y. Liu, Z. Pei, W. Liu, Y. Liu, Z. Tang, W. Zhang, Z. Bo, *Adv. Funct. Mater.*, 2023, **33**, 2301866.
- 28 Y. Zhang, K. Liu, J. Huang, X. Xia, J. Cao, G. Zhao, P. W. K. Fong, Y. Zhu, F. Yan, Y. Yang, X. Lu, G. Li, *Nat. Commun.*, 2021, **12**, 4815.
- 29 J. Y. Fan, Z. X. Liu, J. Rao, K. Yan, Z. Chen, Y. Ran, B. Yan, J. Yao, G. Lu, H. Zhu, C. Z. Li, H. Chen, *Adv. Mater.*, 2022, **34**, 2110569.
- 30 C. Xie, W. Wang, C. Li, Q. Nie, L. Sun, W. Zeng, F. Qin, T. Liu, X. Dong, H. Han, H. Fang, D. Zhao, Y. Zhou, *Adv. Mater. Technol.*, 2021, **6**, 2100181.
- 31 X. Liu, Z. Zheng, J. Wang, Y. Wang, B. Xu, S. Zhang, J. Hou, *Adv. Mater.*, 2022, **34**, 2106453.
- 32 M. R. Ahmadian-Yazdi, M. Eslamian, *Langmuir*, 2021, **37**, 2596.
- 33 Żenkiewicz, M, *J. Achieve. Mater. Manuf. Eng.*, 2007, **24**, 137-145.
- 34 J. R. A. Pearson, *J. Fluid Mech.*, 1958, **4**, 489-500.
- 35 Y. Yue, B. Zheng, W. Yang, L. Huo, J. Wang and L. Jiang, *Adv. Mater.*, 2022, **34**, e2108508.
- 36 M. A. Xenos, E. N. Petropoulou, A. Siokis, U. S. Mahabaleshwar, *Symmetry*, 2020, **12**, 710.

- 37 H. Shi, X. Fu, J. Chen, G. Wang, T. Li, *Hydrolog. Sci. J.*, 2014, **59**, 1856-1871.
- 38 F. Li, Y. Zhao, *Theor. Appl. Climatol.*, 2017, **134**, 397-409.
- 39 C. Guo, Q. Zhang, H. Li, J. Lu, *J. Phys. Chem. C*, 2020, **124**, 18868-18876.
- 40 M. Yao, B. M. Andersson, P. Stenmark, B. Sundqvist, B. Liu, T. Wågberg, *Carbon*, 2009, **47**, 1181-1188.
- 41 J. Jancik, A. Jancik Prochazkova, M. C. Scharber, A. Kovalenko, J. Masilko, N. S. Sariciftci, M. Weiter, J. Krajcovic, *Cryst. Growth Des.*, 2020, **20**, 1388-1393.
- 42 P. W. K. Fong, H. Hu, Z. Ren, K. Liu, L. Cui, T. Bi, Q. Liang, Z. Wu, J. Hao, G. Li, *Adv. Sci.*, 2021, **8**, 2003359.
- 43 T. Xu, J. Lv, K. Yang, Y. He, Q. Yang, H. Chen, Q. Chen, Z. Liao, Z. Kan, T. Duan, K. Sun, J. Ouyang, S. Lu, *Energy Environ. Sci.*, 2021, **14**, 5366-5376.
- 44 M. Sun, K. N. Zhang, J. W. Qiao, L. H. Wang, M. Li, P. Lu, W. Qin, Z. Xiao, L. Zhang, X. T. Hao, L. Ding, X. Y. Du, *Adv. Energy Mater.*, 2023, **13**, 2203465.
- 45 J. Zhang, Q. Huang, K. Zhang, T. Jia, J. Jing, Y. Chen, Y. Li, Y. Chen, X. Lu, H. Wu, F. Huang, Y. Cao, *Energy Environ. Sci.*, 2022, **15**, 4561-4571.
- 46 H. Li, H. Yang, L. Zhang, S. Wang, Y. Chen, Q. Zhang, J. Zhang, H. Tian and Y. Han, *Macromolecules*, 2021, **54**, 10557-10573.
- 47 S. Dong, T. Jia, K. Zhang, J. Jing, F. Huang, *Joule*, 2020, **4**, 2004-2016.
- 48 V. Vohra, K. Kawashima, T. Kakara, T. Koganezawa, I. Osaka, K. Takimiya, H. Murata, *Nat. Photonics*, 2015, **9**, 403-408.
- 49 Y. Wang, X. Wang, B. Lin, Z. Bi, X. Zhou, H. B. Naveed, K. Zhou, H. Yan, Z. Tang, W. Ma, *Adv. Energy Mater.*, 2020, **10**, 2000826.
- 50 X. Ma, G. Ran, H. Li, Y. Liu, X. Cui, H. Lu, Z. Yin, D. Li, H. Zhang, W. Liu, J. Yu, Y. Lin, Y. Liu, W. Zhang, G. Lu, L. Bo, P. Cheng, Z. Ma and Z. Bo, *Adv. Energy Mater.*, 2023, **13**, 2302554.
- 51 J. Fu, P. W. K. Fong, H. Liu, C.-S. Huang, X. Lu, S. Lu, M. Abdelsamie, T. Kodalle, C. M. Sutter-Fella, Y. Yang and G. Li, *Nat. Commun.*, 2023, **14**, 1760.
- 52 J. Yao, T. Kirchartz, M. S. Vezie, M. A. Faist, W. Gong, Z. He, H. Wu, J. Troughton, T. Watson, D. Bryant and J. Nelson, *Phys. Rev. Appl.*, 2015, **4**, 014020.
- 53 H. Chen, R. Zhang, X. Chen, G. Zeng, L. Kobera, S. Abbrent, B. Zhang, W. Chen, G. Xu, J. Oh, S.-H. Kang, S. Chen, C. Yang, J. Brus, J. Hou, F. Gao, Y. Li, Y. Li, *Nat. Energy*, 2021, **6**, 1045-1053.
- 54 W. Sun, H. Chen, B. Zhang, Q. Cheng, H. Yang, Z. Chen, G. Zeng, J. Ding, W. Chen, Y. Li, *Chin. J. Chem.*, 2022, **40**, 2963-2972.
- 55 Y. Huang, H. Chen, Q. Fan, Z. Chen, J. Ding, H. Yang, Z. Sun, R. Zhang, W. Chen, C. Yang, F. Gao, Y. Li, *Chin. J. Chem.*, 2023, **41**, 1066-1074.
- 56 H. Zhang, G. Ran, X. Cui, Y. Liu, Z. Yin, D. Li, X. Ma, W. Liu, H. Lu, R. Liu, L. Cai, W. Zhang, S. Guo, H. Li, J. Yu, Y. Lin, Y. Liu, G. Lu, Z. Ma, P. Cheng and Z. Bo, *Adv. Energy Mater.*, 2023, **13**, 2302063.